Chapter 11
Resonators II: High Frequency Performance and Advanced Applications

11.1 INTRODUCTION

In Chapter 10, we developed closed-form expressions for the motional elements of a crystal resonator containing only a piezoelectric medium. Practical devices consist of a piezoelectric element sandwiched between metal electrodes onto which the electric field is applied. At low frequencies, the primary effect of the metal layers is to lower the series and parallel resonant frequencies rather than to alter resonator performance significantly. Indeed, metal "loading" at low frequencies is the accepted technique for frequency tuning. At higher frequencies, the metal layers begin to constitute an increasingly greater percentage of the overall resonator structure. Because the metal is essentially a "dead" (nonpiezoelectric) layer of low Q (especially for gold and silver), above 100 MHz it begins to degrade device performance by lowering the Q and increasing C_r (because the nonpiezo layer has zero coupling constant, the net k_t^2 of the combination is reduced). In this case, the closed-form expressions (10.63) to (10.73) are no longer valid.

In this chapter, we develop a more complete acoustic description of the thickness-excited metalized resonator, using the one-dimensional Mason model. Metal electrodes are considered as lossy acoustic transmission lines, exactly as in the wideband transducer model. We use the computer program of Figure 6.12 to determine the motional parameters of devices with gold and aluminum electrodes. When compared with the closed-form expression, for example, gold metalization has a much greater effect on resonator Q than aluminum does.

Improvement of resonator Q at high frequencies requires that the metal be removed from the acoustic path. Lateral field excitation (LFE)

is a possible solution, and its full potential has not yet been realized. One reason for this is that computation of the coupling constant is more complicated than in TE due to the increased degree of freedom in which the electrode can be arbitrarily in the resonator plane. We modify the computer program developed in Chapter 4 to determine the coupling constants for LFE modes and to provide curves for quartz and lithium niobate ($LiNbO_3$). Along the principal axes, a cut that is strongly excited in TE will probably not be excited in LFE, and *vice versa*. For example, $LiNbO_3$ has a pure longitudinal mode for the (z)-cut in TE, but exhibits pure shear mode coupling in LFE in this orientation. The coupling constant of this mode is extremely high and has potential applications in wideband devices and resonators.

In the one-dimensional Mason mode, the acoustic propagation vector is in the thickness direction for both TE and LFE modes. Lateral dissipation of acoustic energy, however, is one of the primary factors that degrade resonator performance. This description requires a three-dimensional analysis, so alternative theories have been developed that provide guidelines for the fabrication of high-performance devices. We qualitatively review one of these theories, called *energy trapping*, and apply its conclusions to the design of LFE devices.

Finally, we consider the new area of composite resonators. Composite resonators are structures composed of piezoelectric crystals and substrates in which the thickness and acoustic properties of the substrate are optimized to provide either high Q or low C ratio. The former devices are called HBARs (high overtone bulk acoustic resonators), and the latter devices are known as FBARs (film bulk acoustic resonators).

11.2 MASON MODEL APPROACH TO RESONATOR ANALYSIS AND DESIGN

The one-dimensional Mason model is ideally suited for studying the effect of multiple layers of piezoelectric and nonpiezoelectric materials. Recall that the model yields the complex input impedance, Z_{in}, as a function of frequency. The point where the impedance characteristic crosses the real axis where the resistance is a minimum can be defined as the series resonance, and the zero crossing where the resistance is a maximum is defined as the anti- or parallel resonance. The calculation proceeds as follows:

$$Z_{in}(\omega) = R_m(\omega) + jX_m(\omega) \tag{11.1}$$

where, as usual:

$$X_m(\omega) = \omega L_m - \frac{1}{\omega C_m} \tag{11.2}$$

and L_m and C_m are also functions of frequency (their exact forms are not given by (10.64) and (10.66)). The values of the motional elements depend on the electrical and acoustic parameters of all the layers in the acoustic path. We form the derivative near series resonance, assuming that L_m and C_m are approximately constant in this region:

$$\frac{1}{R_m}\frac{dX_m}{d\omega} = \frac{L_m\omega^2 C_m + 1}{\omega^2 C_m R_m} \tag{11.3}$$

At series resonance, to a good approximation,

$$\omega^2 = \omega_r^2 = \frac{1}{L_m C_m} \tag{11.4}$$

and, therefore,

$$\frac{1}{R_m}\frac{dX_m}{d\omega} = \frac{2}{\omega_r^2 C_m R_m} = \frac{2L_m}{R_m} \tag{11.5}$$

Finally, using (10.67), we obtain

$$Q = \frac{dX_m}{d\omega}\frac{\omega_r}{2R_m} \tag{11.6}$$

As the impedance characteristic approaches the series resonance frequency, we compute the right side of (11.6) to find the device Q. We can define the series resonance in one of two ways:

1. The frequency at which the impedance characteristic crosses the real axis of the Smith chart, i.e., when $X_L = 0$, where $X_L = X_m + 1/j\omega C_0$;
2. The frequency for which the magnitude of the impedance is a minimum.

These two frequencies are not equal due to the presence of the clamped capacitance, but their difference is negligible for high-performance devices.

We will use the first definition here. Having calculated Q, we determine L_m, and C_m from the formulas,

$$L_m = \frac{R_m Q}{\omega_r} \quad \text{and} \quad C_m = \frac{1}{L_m \omega_r^2}$$

To find C_r, we allow the impedance characteristic to continue around the Smith chart until it again crosses the real axis (R_m is a maximum); this is the antiresonance frequency. Finally, knowing ω_r and ω_a, we find that

$$C_r = \frac{\omega_r}{2(\omega_a - \omega_r)} \tag{11.7}$$

Note that because the transducer area, permittivity, and thickness are required in the Mason model, we can calculate C_0 directly and use (10.48) to determine C_r. Comparing the results of both calculations provides a check on the accuracy of the technique. Typically, the variation is less than 2%. The program module that performs these calculations is shown in Figure 11.1. This program is used with the Mason model program (Figure 6.12) and is placed after line 8620. The substrate thickness must be zero for the resonator calculation.

```
8660   IF ABS(F)<.001 AND E<0 THEN GOTO 8860 !RESONANCE CONDITION
8690   IF F<0 AND E>0 THEN GOTO 9260 !ANTIRESONANCE CONDITION
8710   LET PN=N
8740   LET PK=Q
8800   LET Q=Q+R
8830   NEXT S
8860   LET DE=(N-PN)/(Q-PK) !DERIVATIVE OF REACTANCE WITH FREQUENCY
8890   LET QU=DE*Q/(2*M) !EQUATION 11.6
8910   LET LM=(QU*M)/(2*PI*Q) !MOTIONAL INDUCTANCE
8940   LET CM=1/((2*PI*Q)^2*LM) !MOTIONAL CAPACITANCE
8970   PRINT "RESONANT FREQUENCY IS",Q
9000   PRINT "RESISTANCE IS",M
9030   PRINT "Q IS",QU
9060   PRINT "MOTIONAL INDUCTANCE IS",LM
9090   PRINT "MOTIONAL CAPACITANCE IS",CM
9110   LET Q1=Q !SERIES RESONANCE FREQUENCY
9140   LET PN=N
9170   LET PK=Q
9200   LET Q=Q+R
9230   GOTO 8830
9260   PRINT Q1,Q !Q1 AND Q ARE THE SERIES AND PARALLEL RESONANCES
9290   LET CC=Q1/(2*(Q-Q1)) !C RATIO
9310   LET C0=CC*CM !CLAMPED CAPACITANCE
9340   PRINT "THE C RATIO IS",CC
9370   PRINT "THE CLAMPED CAPACITANCE IS",C0
9400   END
```

Figure 11.1 Program listing for calculation of motional elements, Q and C ratio of piezoelectric resonator from electrical impedance characteristic. The program is used with the listing of Figure 6.12.

Example 11.1. Calculate the motional elements of a 10-MHz $\langle AT \rangle$-cut quartz (thickness 1.6×10^{-4} m) resonator with .1-μm gold electrodes using the Mason model and compare with the unelectroded case. The parameters for the $\langle AT \rangle$-cut of quartz are

$$\rho = 2.65, \quad \epsilon_r = 4.5, \quad v_a = 3.3 \times 10^3 \text{ m/s}, \quad k_t^2 = .0077$$

For the unelectroded case, we use the closed-form expressions (10.63), (10.64), and (10.66) (letting $A = 1 \times 10^{-6}$ m^2):

$$Q = 3 \times 10^6, L_m = .15 \text{ H}, R_m = 3.5\ \Omega, C_m = 1.6 \times 10^{-15} \text{ F}$$

For the electroded case, we have, from the computer-aided solution,

$$Q = 2.3 \times 10^6 \quad \text{and} \quad R_m = 4.2\ \Omega$$

Note that the values of the reactive components are identical in the electroded and unelectroded structures. The decrease in the resonator Q in the electroded device results from increased acoustic attentuation in the gold layer, which increases the motional resistance. Practical resonators in this frequency range normally use gold electrodes less than 500 Å thick (just at the point at which the films can be considered continuous) to reduce this attenuation. The electrical resistivity of such films can be quite high and must be carefully balanced against the attenuation requirements.

Table 11.1 shows the motional parameters of an $\langle AT \rangle$-cut fundamental TE mode quartz resonator for several frequencies as a function of the electrode metalization.

In each case, the piezoelectric layer thickness is adjusted so that the structure resonates at the required frequency. In the unelectroded configuration, this thickness corresponds to nearly the half-wave resonance because the C ratio is so large (~140). Notice that with the .2-μm gold electrodes at 1 GHz, the piezoelectric layer thickness must be reduced over 40% to bring the device to the required resonance. The values of L_m and C_m do not vary dramatically between the electroded and unelectroded structures, even at 1 GHz. The decrease in device Q is almost completely a result of the high gold attenuation at this frequency. In the unelectroded case, the device Q is determined only by the material Q, whereas in the electroded case it is a weighted average of the metalization and piezoelectric crystal Q-factors.

Table 11.2 shows the results of similar calculations for $LiNbO_3$ used in the 36° $\langle Y \rangle$-cut. This crystal is characterized by a large coupling constant, high permittivity, and low attenuation, which results in very small motional resistances, especially at high frequencies (Chapter 10). At 1 GHz, the

Table 11.1 Fundamental Mode ⟨*AT*⟩ Quartz

	10 MHz $A = 1 \times 10^{-6}$ m² (1-mm electrode)		
	No Metalization	.1 μm/*Side Gold*	.1 μm/*Side Al*
Q	2.8×10^{6}	1.7×10^{6}	2.6×10^{6}
R_m (Ω)	3.3	5.8	3.7
C_m (F)	2.0×10^{-15}	1.6×10^{-15}	1.8×10^{-15}
L_m (H)	.15	.156	.15
C_0 (F)	2.5×10^{-13}	2.5×10^{-13}	2.5×10^{-13}
d	1.6×10^{-4}	1.57×10^{-4}	1.6×10^{-4}
	100 MHz $A = 8.8 \times 10^{-8}$ m² (12 mil/side)		
Q	220×10^{3}	41×10^{3}	210×10^{3}
R_m	4.1	25	4.7
C_m	1.6×10^{-15}	1.6×10^{-15}	1.4×10^{-15}
L_m	1.4×10^{-3}	1.5×10^{-3}	1.8×10^{-3}
C_0	2.2×10^{-13}	2.5×10^{-13}	2.23×10^{-13}
d	16 μm	14 μm	15.7 μm
	1 GHz $A = 8.8 \times 10^{-8}$ m²		
Q	28.5×10^{3}	3.2×10^{3}	10.6×10^{3}
R_m	.41	2.1	.87
C_m	1.4×10^{-14}	2.4×10^{-14}	1.7×10^{-14}
L_m	1.8×10^{-6}	1.1×10^{-6}	1.5×10^{-6}
C_0	2.2×10^{-12}	3.8×10^{-12}	2.57×10^{-12}
d	1.6 μm	.93 μm	1.36 μm

gold film increases R_m to only 23 mΩ while reducing the Q by a factor of 80. If the *electrical* resistance (R_e) of the film plus bond wires, etc., is 1 Ω, then the device Q will be

$$Q = \frac{\omega L_m}{R_m + R_e} \sim 600 \tag{11.8}$$

Clearly, this is not a very useful device in an oscillator application even though C_r is quite small (under 5 compared with ⟨*AT*⟩ quartz in which it is about 140). Also important is that, because of the small C_r, the resonance frequencies in the unelectroded configuration are far from the half-wave

Table 11.2 Fundamental Modes for $LiNbO_3$ (y)-cut

	No Metalization	.1 μm/*Side Gold*	.1 μm/*Side Aluminum*
	10 MHz	$A = 1 \times 10^{-6}$	
Q	25×10^6	1.0×10^7	24×10^6
R_m	3.3×10^{-3}	7×10^{-3}	3.0×10^{-3}
C_m	2.2×10^{-13}	2.4×10^{-13}	2.2×10^{-13}
L_m	1.1×10^{-3}	1.1×10^{-3}	1.2×10^{-3}
C_0	1×10^{-12}	1.1×10^{-12}	1.03×10^{-12}
d	335 μm	330 μm	335 μm
	100 MHz	$A = 8.8 \times 10^{-8}$	
Q	2.5×10^6	1.6×10^5	1.7×10^6
R_m	3.2×10^{-3}	48×10^{-3}	4.7×10^{-3}
C_m	1.9×10^{-13}	2×10^{-13}	2×10^{-13}
L_m	1.3×10^{-5}	1.2×10^{-5}	1.3×10^{-5}
C_0	9.1×10^{-13}	9.2×10^{-13}	9.2×10^{-13}
d	33 μm	32.5 μm	33 μm
	1 GHz	$A = 8.8 \times 10^{-8}$	
Q	200×10^3	2.6×10^3	45×10^3
R_m	3×10^{-4}	23×10^{-3}	1.7×10^{-3}
C_m	1.7×10^{-12}	2.6×10^{-12}	2.0×10^{-12}
L_m	1×10^{-8}	9.7×10^{-9}	1.2×10^{-8}
C_0	9×10^{-12}	12×10^{-12}	9.3×10^{-12}
d	3 μm	2.6 μm	3.2 μm

frequencies. Because $v_a = 7.4 \times 10^3$ m/s, the *antiresonances* are given by 370 μm, 37 μm, and 3.7 μm at 10 MHz, 100 MHz, and 1 GHz, and the series resonances are reduced to 335 μm, 33 μm, and 3.0 μm, respectively. Note that the reduction is independent of the operating frequency range. From the table, we find that $C_r \sim 4.6$, and (10.48) yields a value of 4.9. Recall that for very small C_r the derivation of (10.48) breaks down because the tangent function cannot be expanded around its poles.

11.3 TECHNIQUES FOR IMPROVING RESONATOR Q

11.3.1 BVA

Because the main Q detractor at high frequencies is the metallic loading performance, improvements center on the elimination of the electrodes from the acoustic path. One such technique, called BVA, is illustrated in Figure 11.2. (BVA means "in a small box" in French.) The electrodes are separated from the crystal by a distance d', which is made as small as possible. At frequencies of a few megahertz, Q-factors approaching the material limit for quartz have been reported [4, 5]. The problem is that the configuration adds a series capacitor, which, as we have previously shown, increases the C ratio. This problem increases in severity as the frequency increases. To be useful at 1 GHz, for example, the gap between the crystal and electrode must be extremely small, and special fabrication techniques are necessary. Typical gaps at 2 to 5 MHz are in the 1 to 2 mil range.

The BVA resonator "looks" like a resonator crystal in series with an air gap capacitor, as in Figure 10.9. It is convenient to absorb this capacitor into the Butterworth-Van Dyke (BVD) circuit as shown in Figure 11.3. It is not difficult to show that

$$\begin{aligned} L'_m &= \left(\frac{C_S + C_0}{C_S}\right)^2 L_m, \quad C'_0 = \frac{C_S}{C_0 + C_S} C_0 \\ R'_m &= \left(\frac{C_S + C_0}{C_S}\right)^2 R_m, \quad C'_m = \frac{C_S^2}{(C_S + C_0)(C_m + C_S + C_0)} C_m \end{aligned} \tag{11.9}$$

The C ratio of the BVA resonator is

$$\frac{C'_m}{C'_0} = C'_r = \frac{C_m + C_S + C_0}{C_S} C_r \approx \frac{C_S + C_0}{C_S} C_r$$

The increase in motional resistance depends on the square of the ratio of the clamped capacitance to the air gap capacitance, whereas the increase in the C ratio depends linearly on the same ratio. Thus, for a high coupling crystal, it should be possible to use this technique to raise the resistance to a reasonable level with only a moderate increase in the C ratio. When this technique is used with low coupling crystals such as quartz, we usually employ a third or fifth harmonic. In this design, the effect of the gap can be made negligible because C_0 will generally be smaller than C_S. There is another advantage of overtone design in electrodeless resonators, which we will investigate later.

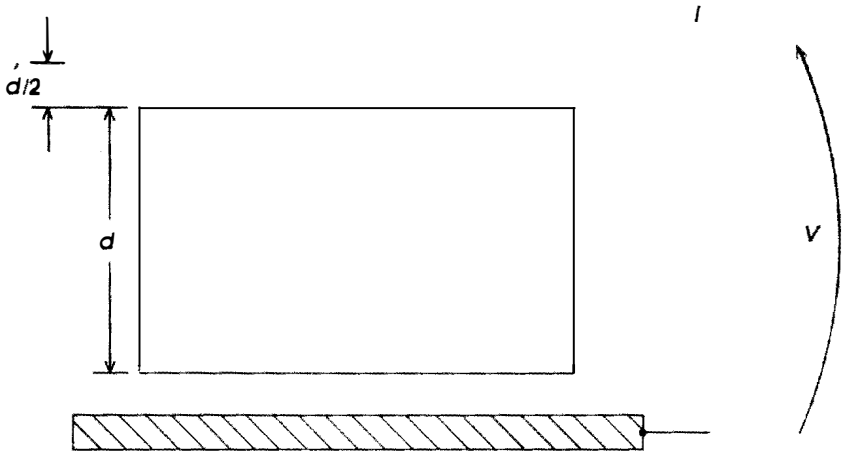

Figure 11.2 BVA structure. The electrodes are physically separated from the crystal by a gap of dimension d'.

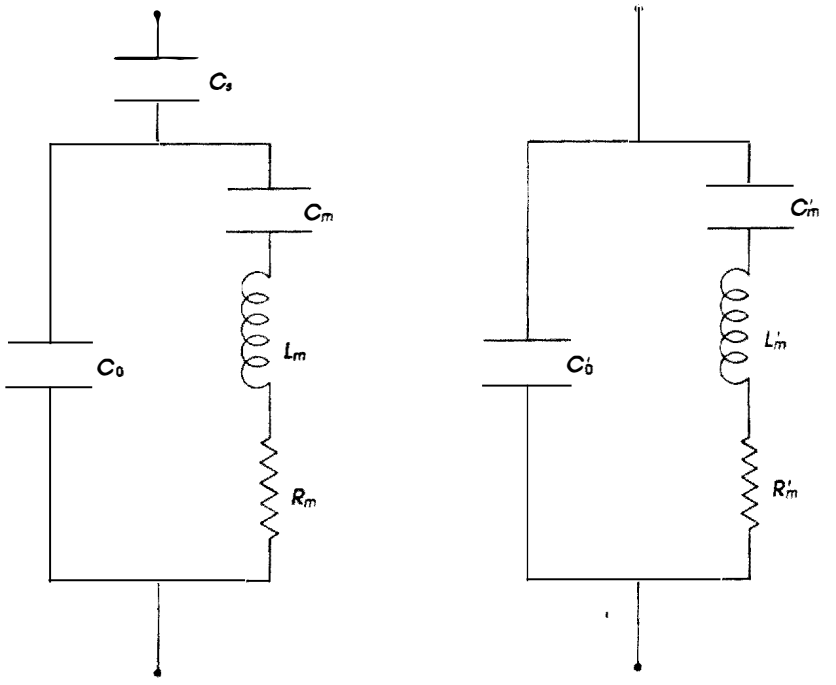

Figure 11.3 Equivalent of BVA structure to the BVD circuit. The circuit values are given in (11.9).

Example 11.2. Compute the BVA C ratio and motional resistance for a 1 GHz $LiNbO_3$ resonator with a 3-μm air gap. Let $A = 8.8 \times 10^{-8}$ m^2, $C_S = 2.6 \times 10^{-13}$, and $C_0 = 9 \times 10^{-12}$. From (11.7),

$$C_r \sim 5 \quad \text{and} \quad C_r' = 36C_r = 180$$

and

$$R_m' = 1300R_m = .39\ \Omega \quad \text{if} \quad R_m \text{ is } .3\ \text{m}\Omega$$

The electrodeless design has increased the motional resistance to a level where the resonator could be potentially useful while the C ratio is still reasonable.

11.3.2 Lateral Field Excitation

Lateral field excitation is also an "electrodeless" technique, because the metallic layers are not in the acoustic path. The resonator Q, in theory, should be identical to the material Q at all frequencies, and no special fabrication techniques are required at high frequencies. The C ratio is not necessarily higher than in TE, because the coupling constant, which depends on the orientation, is comparable for LFE and TE. An important difference between the two types of excitations is that in LFE the clamped capacitance is difficult to calculate and, for most practical examples, is dramatically less than the TE case. Because the gap between the electrodes (see Figure 10.4) is a variable, an extra degree of freedom has been introduced to control the motional resistance (in the TE case, only the electrode area determines C_0). For LFE devices reported in the literature, C_0 is typically two to three orders less than comparable TE resonators. Because C_r depends only on K^2 and it is clear that the motional capacitance is also dramatically less in LFE, the motional *inductance* is dramatically increased. Finally, because the Q has not been degraded (it should actually be significantly higher, especially at high frequencies), the motional resistance should be much higher (from (10.62)). A typical motional resistance (e.g., at 5 MHz) may be as high as 6 kΩ for AT quartz for the *series* resonance! If very high coupling, high dielectric materials are used, however, the motional resistance should be much lower. Furthermore, the clamped capacitance does not increase linearly with frequency as it does in the TE case because it is not inversely proportional to the resonator thickness. Thus, the motional resistance should not decrease with frequency to the ridiculously low levels that are predicted by the Mason model for TE resonators for which we can increase the resistance only by using

very small transducer areas, which are difficult to fabricate and produce serious nonlinear effects. Using LFE designs, we should be able to fabricate devices at microwave frequencies with reasonable motional resistances and high Q-factors.

11.4 CALCULATION OF K^2 FOR LATERAL FIELD MODES

In Chapter 4, we developed a technique for calculating the coupling constant of a piezoelectric crystal. The technique requires us to calculate the phase velocity by using the *stiffened* stiffness constants and the unstiffened constants and forming the difference in the velocities. To calculate the coupling constant in the LFE case, we perform a similar operation, but we require that the components of the electric field perturbation (the *stiffened* component) be perpendicular to the direction of acoustic propagation.

To understand the technique, consider the Christoffel matrix:

$$\Gamma_{ij} = l_{iK} c_{KL} l_{Lj}$$

where l_{iK} and its transpose l_{Lj} depend only on the acoustic propagation direction. The full *stiffened* Christoffel matrix is

$$\Gamma_{ij} = l_{iK}\left(c_{KL} + \left[\frac{(e_{Kj}l_j)(l_i e_{iL})}{l_i \epsilon_{ij}^S l_j}\right]\right) l_{Lj}$$

The stiffening correction term (in brackets) involves the vectors l_i and l_j, which correspond to the orientation of the acoustically generated electric field. In TE, these vectors are oriented in the direction of acoustic propagation. In LFE, l_i and l_j are in the direction of the external electric field, which can be oriented arbitrarily in the plane perpendicular to the acoustic propagation, and are no longer fixed by l_{iK} and l_{Lj}. Recall that, in the TE case, we allowed the propagation direction (i.e., the crystal cut) to vary between predefined orthogonal axes in a Cartesian system. This procedure, outlined in Chapter 4, produced curves for the electromechanical coupling constant, as shown in Figures 4.8 to 4.10. In the LFE case, the procedure is similar, except that there is an extra degree of freedom.

Example 11.3. Calculate the possible lateral field coupling constants for $\langle z \rangle$-oriented barium sodium niobate.

Because acoustic propagation is in the z direction the electric field must be in the xy plane. First consider a y-directed field. We form the matrix products $e_{Kj}l_j$ and $l_i e_{iL}$:

$$l_i e_{iL} = \begin{bmatrix} 0 \\ 0 \\ 0 \\ e_{24} \\ 0 \\ 0 \end{bmatrix} \quad \text{and} \quad e_{Kj} l_j = [0\ 0\ 0\ e_{24}\ 0\ 0]$$

and

$$l_i \epsilon_{ij} l_j = e_{22}$$

The stiffened Christoffel matrix is

$$\Gamma = \begin{bmatrix} c_{55} & 0 & 0 \\ 0 & c'_{44} & 0 \\ 0 & 0 & c_{33} \end{bmatrix}$$

where

$$c'_{44} = c_{44} + \frac{e_{24}^2}{\epsilon_{22}}$$

As expected, the piezoelectrically active mode is a shear wave, and the coupling constant is

$$K^2 = \frac{e_{24}}{\epsilon_{22} c_{44}} = K_y^2$$

It is easy to show that had the field been oriented in the x direction, the coupling constant would be

$$K^2 = \frac{e_{15}^2}{\epsilon_{11} c_{55}} = K_x^2$$

For a given plate orientation, the coupling constant depends on the direction of the electric field. As the field is rotated around the plate normal, the coupling constant varies sinusoidally from K_y^2 to K_x^2.

If the resonator itself is allowed to rotate, then three general cases must be considered:

1. The electric field is fixed relative to the coordinate axes while the plate normal ($\hat{\mathbf{N}}$) is rotated around **E**. This geometry is illustrated in Figure 11.4(a).

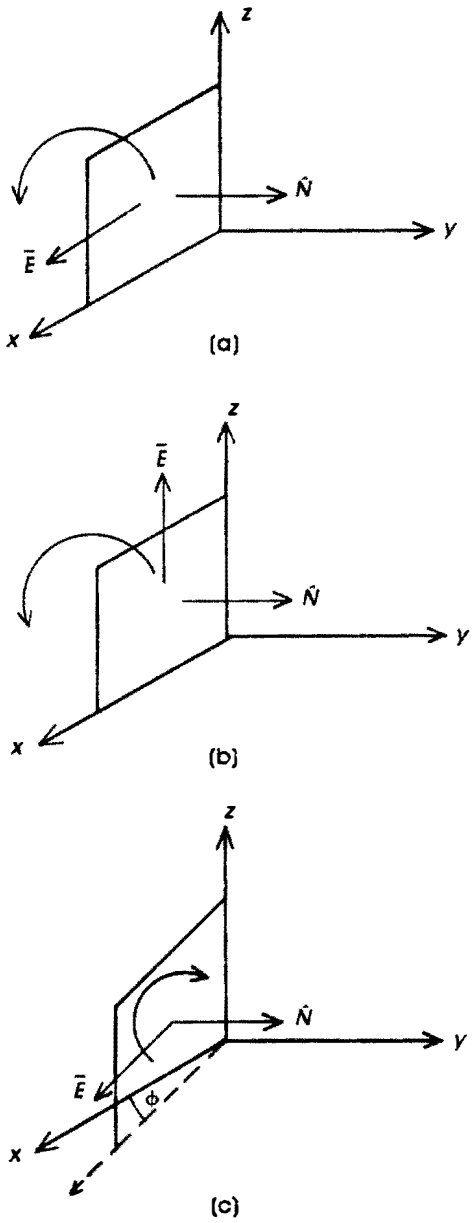

Figure 11.4 Lateral field excitation configurations. There are three general cases defined by the direction of the electric field with respect to the plate normal (**N**). In all cases, **E** is perpendicular to **N**.

2. The electric field and plate normal are rotated together about an axis normal to both, as shown in Figure 11.4(b).
3. The plate normal is fixed with respect to the coordinate axes, and the electric field is rotated in a plate normal to $\hat{\mathbf{N}}$, as shown in Figure 11.4(c). This case is especially important if the particular cut is known to be, e.g., stable with respect to a temperature-independent $\langle AT \rangle$-cut or a vibration-insensitive $\langle SC \rangle$-cut.

We treat each of these cases separately in the computer programs by defining a vector **M13** (e.g., in Figure 3.1) in line 2680 independently of **L13**. This allows the stiffness correction to be decoupled from the propagation direction. For TE modes, **M13** = **L13**; for LFE modes, **M13** is required to be perpendicular to **L13**.

We consider the first geometry for crystal quartz in which the electric field is x-directed and the platelet is rotated about the x-axis. The program modifications are

Abscissa: 0, 1, 0
Ordinate: 0, 0, 1
M13: 1, 0, 0

The results of this calculation are shown in Figure 11.5. We see that at Y-35° (the AT-cut) there are two excited modes; the pure shear mode (c mode) is strongly excited, as is the quasilongitudinal (a mode). For a given plate thickness, we can easily find the frequencies of the two modes from the Christoffel equation by using the stiffened stiffness components. The phase velocity of the pure shear mode is 3.32×10^3, equal to the TE case (because $k_t^2 \sim K^2$), and the longitudinal mode has a velocity about 25% higher. This mode will show up as a spurious response, but because the frequency is not in the inductive region of the resonator (the C ratio is quite large), it will probably not cause severe problems.

The BT-cut possesses two moderately excited modes, the quasishear and the quasilongitudinal. This cut is thus not particularly useful. We note that at 90° and 156°, the coupling constant jumps between the b and c modes. These discontinuities are shown explicitly to be consistent with resonator terminology in which the a, b, and c modes represent the longitudinal, fast shear, and slow shear modes, respectively. Thus, at a shear degeneracy, the mode will shift from slow to fast (or *vice versa*); however, the coupling constant curve is continuous. The same discontinuities occur in TE (and at the same angles). They were shown in Figure 10.14, but not in Figure 4.9, for $LiNbO_3$ in the yz plane to emphasize that piezoelectric coupling occurs only for the quasishear mode (which can be either the b mode or the c mode, depending on the crystal cut).

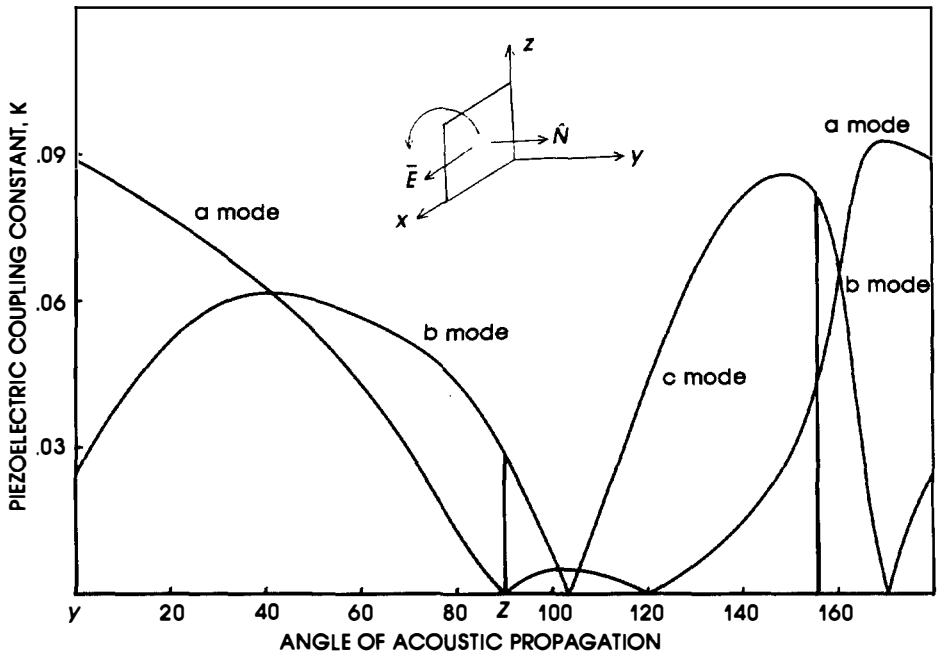

Figure 11.5 Lateral field excitation in quartz. The resonator plate rotates in the yz plane while the field is along the x-axis. The discontinuities occur at shear degeneracies.

For the second geometry, **E** and $\hat{\mathbf{N}}$ rotate together about the x-axis. The relevant modification is

Abscissa: 0, 1, 0
Ordinate: 0, 0, 1
M13: $(0, -\sin\theta, \cos\theta)$

For an arbitrary angle in the yz plane, $\hat{\mathbf{N}}$ and **E** are normal to each other, and both are perpendicular to the x-axis (1, 0, 0). The results of this geometry are shown in Figure 11.6. At the (AT)-cut, only the pure shear mode is excited, whereas at the (BT)-cut angle only the quasishear mode is excited. Again, the discontinuities are due to the shear degeneracies at 90° and 156°.

The third case is the structure in which the plate normal is fixed and **E** is rotated about it. For the (AT)-cut, we let $\hat{\mathbf{N}}$ form an angle of 35° with the y-axis:

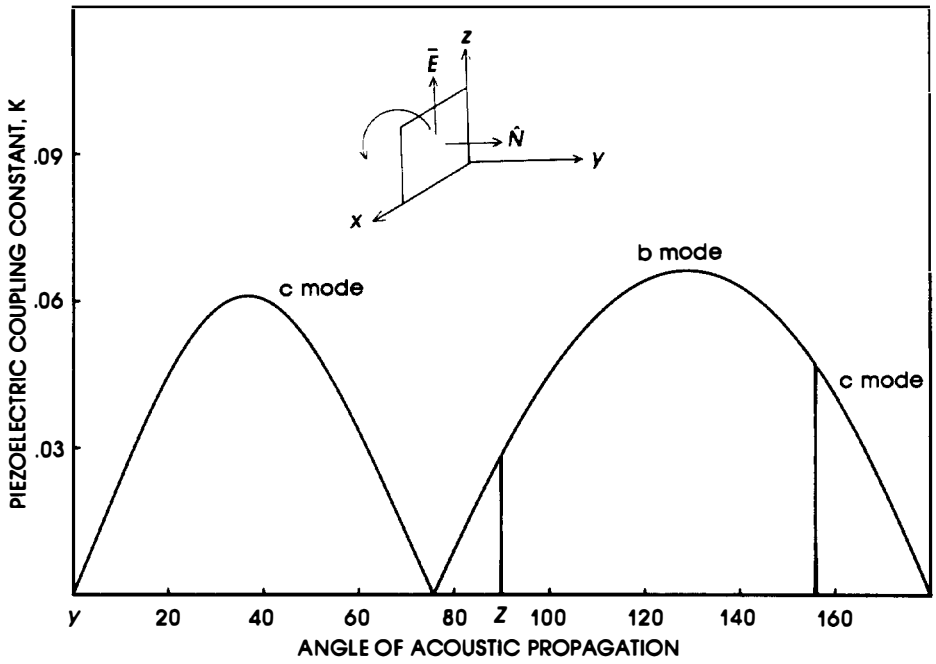

Figure 11.6 Lateral field excitation in quartz in the yz plane in which **E** is normal to the x-axis.

$$\begin{aligned} &L13(1,1) = 0 && \text{Abscissa: } (1, 0, 0) \\ &L13(1,2) = \cos\theta = .817 && \text{Ordinate: } (0, -.577, \overset{+}{-}.817) \\ &L13(1,3) = \sin\theta = -.577 \end{aligned}$$

This notation conforms to that of [7] and is used in Figures 11.7 to 11.9. Because **L13** is fixed, the matrices l_{iK} and l_{Ki} are also constant. The electric field rotates about **L13**. Figure 11.7 shows that coupling constant for this situation.

Example 11.4. An extremely important case is that of the *SC*-cut. From Figure 11.8, we have

$$\hat{\mathbf{N}} = -\sin\phi\cos\theta\hat{\mathbf{i}} + \cos\phi\cos\theta\hat{\mathbf{j}} + \sin\theta\hat{\mathbf{k}} \tag{11.10}$$

The electric field rotates from the x' to the z', which are defined as

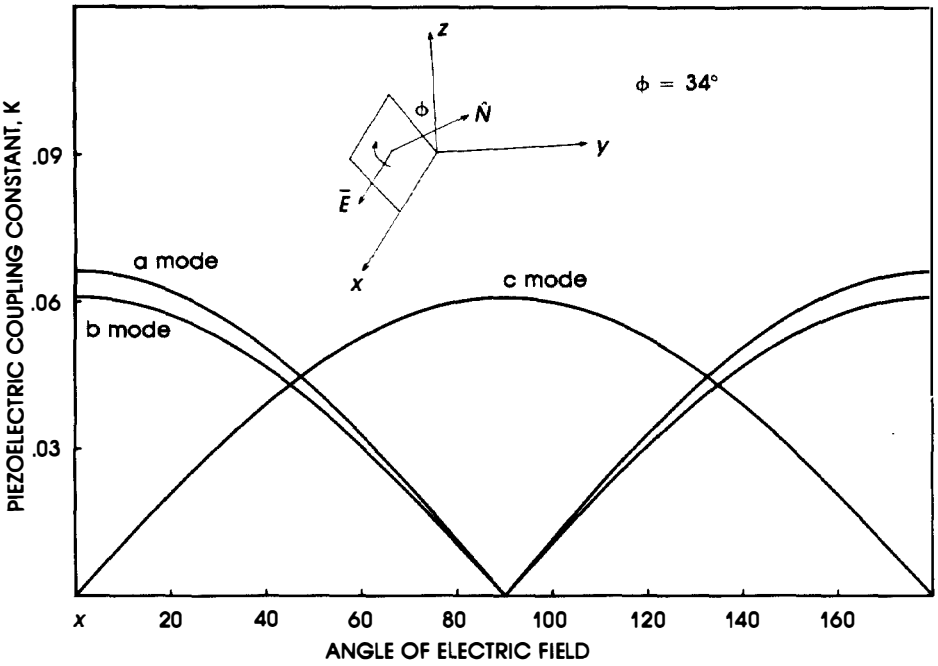

Figure 11.7 Lateral field excitation in quartz for the $\langle AT \rangle$-cut with **E** rotating in the plane of the resonator plate; 0° corresponds to the x-axis.

$$x' = \cos\phi\hat{\mathbf{i}} + \sin\phi\hat{\mathbf{j}}$$

$$z' = -\sin\theta\sin\phi\hat{\mathbf{i}} + \cos\phi\sin\theta\hat{\mathbf{j}} - \cos\theta\hat{\mathbf{k}}$$

For this doubly rotated cut, we make the following modifications to the computer program:

L13(1, 1) = −.316
L13(1, 2) = .767
L13(1, 3) = .558
Abscissa: (.924, .381, 0)
Ordinate: (.213, −.516, .83)

As in Figure 11.7, **L13** defines the plate normal that is fixed in position.

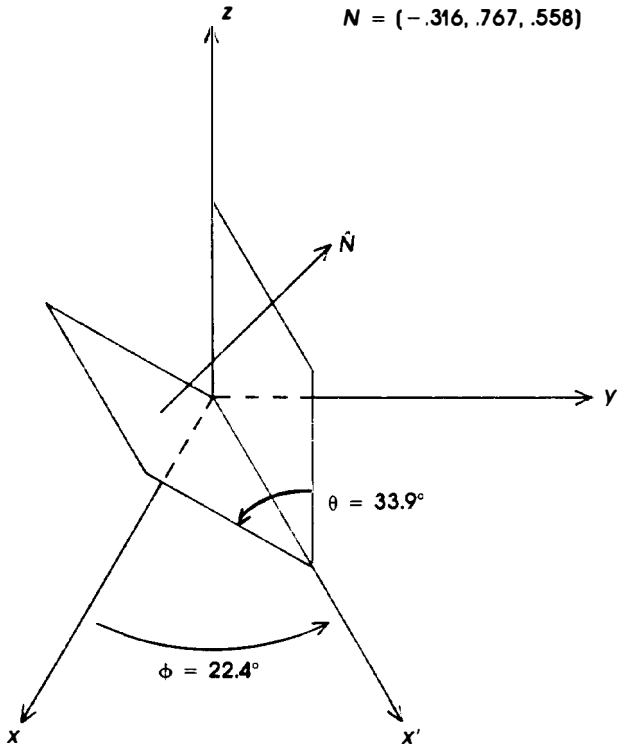

Figure 11.8 The stress-compensated orientation is a doubly rotated cut specified by two angles, θ and ϕ.

The coupling constant is shown in Figure 11.9. Compared with the thickness-excited structure in which all three modes are piezoelectrically active, we see that, if the electric field is oriented along an axis $-60°$ from x', only the c mode is strongly excited. The ability to excite any mode by adjusting the direction of the electric field is a consequence of the extra degree of freedom inherent in LFE.

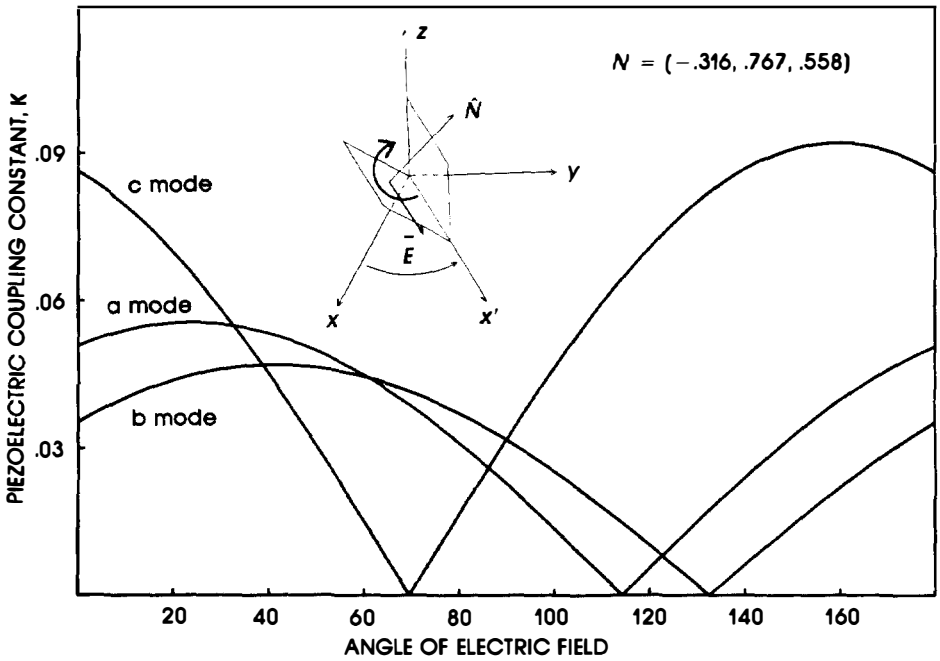

Figure 11.9 Lateral field excitation in quartz for the ⟨*SC*⟩-cut. The electric field rotates in the resonator plane with 0° corresponding to the x'-axis (see Figure 11.8).

11.5 LATERAL FIELD EXCITATION IN LITHIUM NIOBATE

As we have seen, $LiNbO_3$ possesses cuts with very high coupling in TE. We now investigate the coupling constants for LFE. Figure 11.10 shows the LFE modes in the yz plane. In this figure, the electric field is oriented along the x-axis. The z-propagating shear wave possesses a coupling constant of .78, which is the highest value for a single-crystal material (it is over 15% higher than the ⟨x⟩-cut TE mode). This value is consistent with the reported data of Ballato [8]. An additional advantage of this

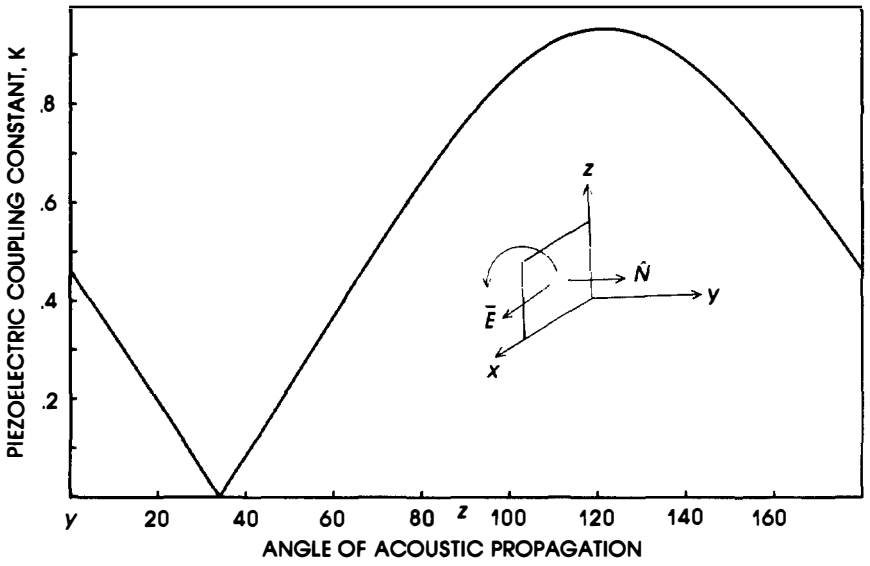

Figure 11.10 Lateral field excitation in $LiNbO_3$ for rotated y-cut with the electric field in the x direction; 0° corresponds to the y-axis, 90° to the z-axis. Recall that the z-cut in TE possessed only a pure longitudinal mode, whereas in LFE it has only a pure shear mode with extremely high coupling.

structure over the $\langle x \rangle$ TE orientation is that the b mode is the only piezoelectrically excited mode present. At 121°, the value rises to .94. Utilizing this mode in wideband devices could result in dramatically improved performance.

It is not difficult to show that the z-cut $LiNbO_3$ for an LFE structure is independent of the orientation of **E**. This property relaxes fabrication difficulties. For the 121° cut, the coupling depends on electric field direction, and the maximum value occurs for orientation along x.

11.6 ENERGY TRAPPING AND SPURIOUS RESPONSES

The one-dimensional Mason model predicts the performance of resonators with arbitrary acoustic and electrical properties and is especially useful for modeling metalized devices at high frequencies. However, important experimental results cannot be explained by a one-dimensional model, such as:

1. Resonator Q is at times significantly lower than predicted with thin metalizations, expecially in fundamental mode operation;
2. C ratio can also be significantly lower than predicted under the same conditions;
3. Spurious responses appear in the inductive region, which severely degrade device performance.

The origin and resolution of these phenomena require a three-dimensional analysis, which is difficult even for the simplest configurations because, generally, the acoustic materials are anisotropic and described by complex matrices and the boundary conditions involve complex stress and strain components. Historically, the three-dimensional problem has been attempted by a semiquantitative approach called *energy trapping theory*. This is the approach considered here. For further simplicity, we consider a two-dimensional model that contains most, if not all, of the physical features of the full three-dimensional analysis.

To get a qualitative feel for the concept of energy trapping, we first consider the presumably more familiar problem of a symmetric dielectric optical slab waveguide, as shown in Figure 11.11. The guide is very wide, so there is no field variation in the y direction. The core and cladding indices of refraction are n_1 and n_2, respectively, with $n_1 > n_2$. This structure contains transverse electric and transverse magnetic modes. Refer to Figure 11.11; of the two optic beams, beam 1 is partially refracted and partially reflected at the top boundary while beam 2 undergoes total internal reflection. Thus, beam 1 attenuates (it is called an evanescent mode) and beam 2 propagates along the guide axis. The *critical* angle above which a beam will propagate unattenuated is

$$\sin\alpha_c = \frac{n_2}{n_1}$$

For a glass guide, bounded by air, $\alpha_c \approx 42°$. If the beam is incident at an angle smaller than α_c, it will be "cut off" and dissipate in the cladding material. Because α is the angle between the z- and x-propagation constants, it cannot be chosen arbitrarily. We determine α by solving the two-dimensional wave equation and by invoking the continuity of the tangential electric field at the top and bottom interfaces. The angle α involves the relation between the optic wavelength λ to the thickness d of the guide. It is intuitively clear that the larger d is in relation to λ, the farther the beam is from cutoff and the larger is the angle α.

Now consider an analogous model for the acoustic resonator configuration shown in Figure 11.12. This model has aspects of the dielectric

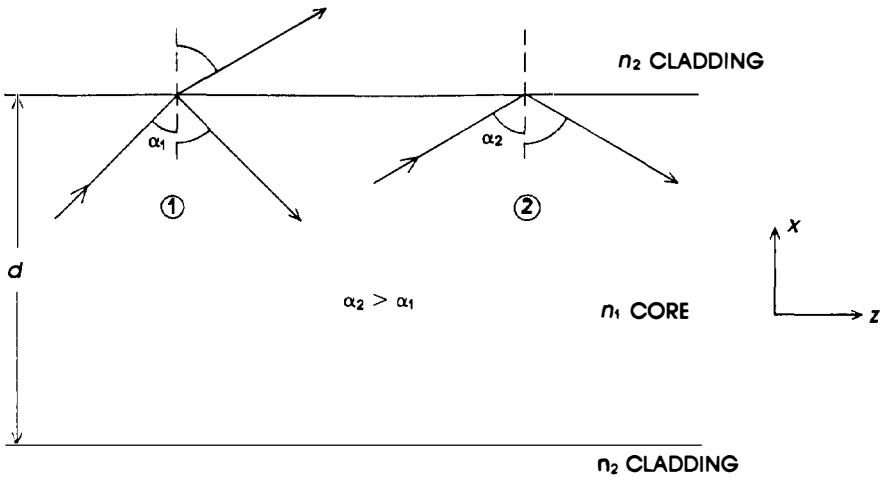

Figure 11.11 Geometry of symmetric slab optical waveguide. Ray 1 is not totally internally reflected and is not guided. Ray 2 is totally internally reflected and propagates in the core without attenuation.

waveguide as well as properties of a microwave cavity. Two regions, labeled *e* and *s*, represent the electroded and unelectroded regions of the resonator. At the top and bottom boundaries of both regions, the acoustic waves are totally reflected, whereas at the *e-s* interface the wave is either reflected or transmitted, depending on the difference between acoustic properties of the two regions. The acoustic phase velocity in the two regions is identical (unlike the optic waveguide), but, due to electrode mass loading, the electroded region can be considered as having a larger dimension and, thus, a lower cutoff frequency. The mass loading, which depends on the properties and thicknesses of the metal electrodes, is thus analogous to the index ratio n_1/n_2 in the optic guide. To satisfy the boundary condition requires an x component in the propagation vector. Physically, this component arises because the electroded region, which makes up a tiny portion of the transducer platelet, can be considered as the impact area of a large drum. An external field causes waves that propagate in the lateral (i.e., along x) and thickness directions. If the mass loading relative to d is large enough, the wave is completely confined to the electroded region, just as the optic wave is confined to the core for large index ratios.

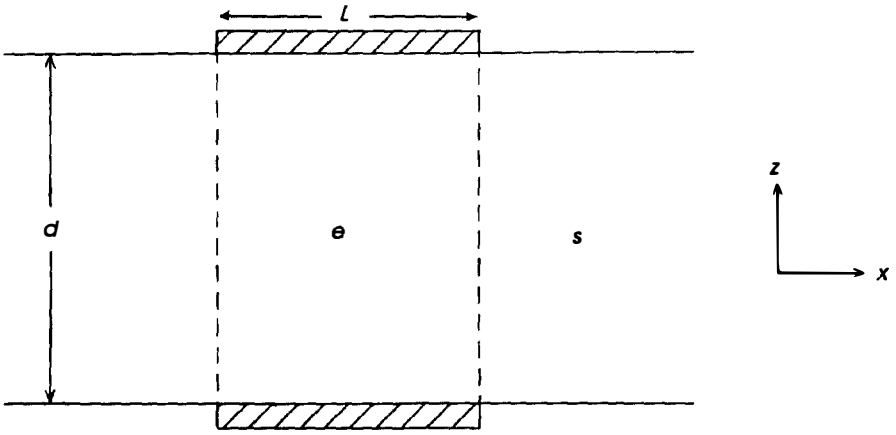

Figure 11.12 An acoustic resonator in TE consists of two regions labeled *e* (electroded) and *s* (unelectroded). Trapped energy modes are confined to region *e* just as guided optical rays are confined to the core of the slab guide.

Alternatively, we can think of the wave as propagating in region *e* but being cutoff in region *s*. This is the energy-trapped structure. In this case, the one-dimensional model accurately predicts resonator characteristics. On the other hand, if the mass loading is negligible (analogous to $n_1 \approx n_2$), there is no mechanism to confine the acoustic beam to the electroded region. The beam is thus free to propagate into the unelectroded region, which results in a dramatically reduced Q and a higher C ratio. In this case, the mode is untrapped, and its characteristics cannot be determined from a one-dimensional model.

In normal resonator operation, the modes are indeed trapped, and the electroded region acts as an acoustic cavity. The cavity modes are solutions of the wave equations, with reflecting walls at the top, bottom, and lateral boundaries. The eigenfrequencies are thus given by

$$f_{NM} = \frac{v_a}{2}\left[\left(\frac{N}{d}\right)^2 + \left(\frac{M}{L}\right)^2\right]^{1/2}, \quad M, N = 1, 3, 5, \ldots \tag{11.11a}$$

If L (which is the lateral direction of the electroded region) is very large, (11.11a) reduces to (10.35). We also assume, when writing (11.11a), that the difference between resonance and antiresonance frequencies is small

$(k_t^2 \ll 1)$. Usually, $d \ll L$ and (11.10) can be written as

$$f_{NM} = \frac{v_a N}{2d}\left[1 + \left(\frac{1}{2}\frac{Md}{LN}\right)^2\right] \tag{11.11b}$$

For each harmonic mode N, there are a series of *inharmonic* modes given by $M = 1, 3, 5, \ldots$ with frequencies above the frequency of the main resonance. These modes represent the spurious resonances that generally will be present for a given harmonic N. They also represent, primarily, thickness propagating modes with small propagation components in the lateral direction. If we trap the main mode, we automatically trap the inharmonic modes. In the $\langle AT \rangle$-cut, there is a set of modes that has propagation vectors primarily in the lateral direction. These are LFE modes, and they occur because the $\langle AT \rangle$-cut is a rotated orientation, so a single electric field will generally excite both TE and LFE modes (recall that in both the $\langle AT \rangle$- and $\langle SC \rangle$-cuts TE and LFE modes are present). In the $\langle AT \rangle$-cut, these modes are called *thickness twist modes*, and their frequency spectrum can be above or below the fundamental thickness mode.

The strengths of the spurious modes are complex functions of the boundary conditions, but can be comparable to the main mode. Equation (11.11b) provides a technique by which the spurs can be removed from the operating region at least, if not eliminated completely. We note that the frequency separation between the inharmonic modes is inversely proportional to L; hence, decreasing the resonator dimension allows the spurs to be moved far enough away from the main resonance that they do not interfere with the device operation.

For higher-order harmonic numbers (N), the angle of the acoustic propagation vector tilts away from the lateral direction. This situation is identical to Figure 11.11, in which the propagation at higher frequencies tends to be directed along the waveguide axis. Thus, less metalization is required to trap the energy. A mode may be untrapped in the fundamental mode and trapped at the third and higher harmonics.

To summarize: The metal electrodes provide for the trapping of energy in the electroded region. If the electrodes are very thin or not present, trapping depends entirely on the anisotropy of the crystal, which may or may not be sufficient to confine the acoustic wave. Along with the fundamental mode, the inharmonic (spurious) modes are also trapped. Even though they are generally much weaker than the main mode, inharmonic modes can cause severe problems in normal device operation. To alleviate the effect of the spurs, we must reduce the electrode dimensions sufficiently so that the frequency separation of the first spur falls outside the operating region.

In the BVA structure, there is no metalization touching the resonator surface. Trapping can be accomplished by sputtering a low attenuation dielectric layer in the acoustic path, by reducing the thickness of the region surrounding the path, or by operating in a higher-order harmonic. In LFE, the metalization is in contact with the resonator but it is outside the acoustic path, and thus the problem is even more severe than in the BVA structure. Techniques proposed to promote trapping include recessing the electroded region (by controlled chemical etching or ion beam milling) and operating in a higher-order harmonic.

11.7 COMPOSITE RESONATORS

For most applications, especially at frequencies less than 100 Mhz, the traditional thickness-excited mode operation using quartz is quite satisfactory. Recently, however, interest has focused on two potentially important applications that cannot be satisfied by thickness-excited quartz. Both involve structures that contain piezoelectric layers as well as nonpiezoelectric layers, in which the "dead" layer forms an appreciable part of the acoustic path to the extent that it determines the device properties. Such devices are appropriately called *composite* resonators. We analyze composite resonators in the same way as we analyze metalized resonators by simply modifying the thicknesses of the various layers of the one-dimensional Mason model.

11.7.1 High Overtone Bulk Acoustic Resonators

For very high frequency operation in which a high Q is required, a low-loss nonpiezoelectric crystal cavity is attached to the piezoelectric layer as shown in Figure 11.13. The structure utilizes standing waves, which are always present in a low-loss substrate, to produce an acoustic Fabry-Perot interferometer. The structure consists of two coupled cavities. The function of the transducer is to couple a small amount of energy into the high-Q cavity without introducing appreciable acoustic loss, and the transducer is usually an extremely small part of the total acoustic path length. The device Q is thus nearly equal to the material Q of the acoustic cavity. Furthermore, because the acoustic cavity is very large compared with the acoustic wavelength (the transducer thickness is one half wavelength), the device operates at a very high harmonic of its fundamental. Such devices are called *high overtone bulk acoustic resonators* (HBARs). The device C ratio is thus extremely large. The response consists of a series of resonances and antiresonances with frequency separation inversely proportional to the

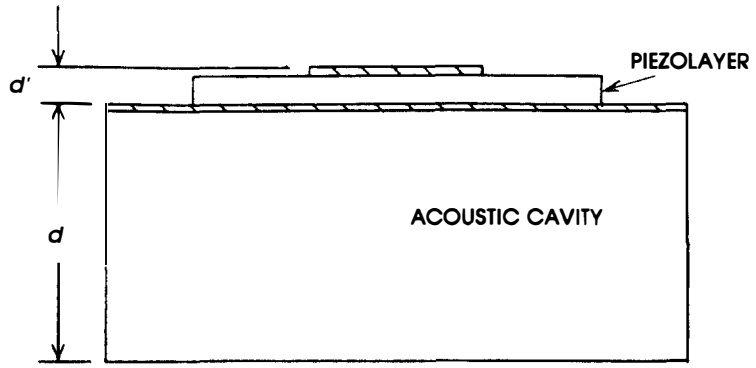

Figure 11.13 HBAR configuration. The substrate (thickness $d \gg d'$) is a very low attenuation crystal, and the response is a series of very high Q resonances.

cavity length d, as given by the Fabry-Perot formula (compare with Figure 6.16),

$$\Delta f = \frac{v_a}{2(d' + d)} \tag{11.12}$$

Increasing d will generally increase the device Q, but will cause the resonances to be spaced closer together. Typical values of d and d' at 1 GHz are $d' = 2 - 3$ μm and $d = 1 - 2$ mm. From (11.12), the frequency spacing is in the range of 1 to 4 MHz. Good choices for the acoustic cavity crystal are YAG (yittrium aluminum garnet), spinnel ($MgOA_2O_3$), and sapphire (crystal Al_2O_3).

An HBAR can be a single-port device, in which case it is used very much like an ordinary resonator, or a two-port device. In the latter case, it is characterized by its insertion loss (IL) as well as its Q. Usually Q cannot be maximized without increasing the IL, because a high Q requires a poor acoustic match between transducer and acoustic cavity. Insertion losses of less than 10 dB with Q-factors greater than 100×10^3 have been achieved at 1 GHz by using sputtered ZnO on YAG, and HBARs in the frequency range from 300 MHz to over 2 GHz are easily fabricated. Frequencies below 300 MHz require very thick piezoelectric layers, which are difficult to fabricate with sputtered films. Bonded transducer technology is preferred in this frequency range, even though it is not compatible with large-scale production.

Because the HBAR exhibits a large spectrum of very high Q resonances, it may be possible to stabilize an oscillator over any one of several frequencies that may be chosen on demand. One of the main advantages of this approach is that the stabilization is performed directly at microwave frequencies without the need for the frequency multiplication required with conventional quartz resonators operating at low fundamental frequencies. High overtone acoustic devices operating near X band have been reported.

The possible Q detractors are

1. Attenuation in the acoustic cavity,
2. Attenuation in the transducer,
3. Diffraction spreading in the cavity,
4. Surface roughness and lack of cavity parallelism,
5. Attenuation in the ground plane.

The Q of a typical HBAR crystal is normally above 200×10^3 at 1 GHz, and thus cavity attenuation is usually not important. The Q of the transducer (if ZnO) is at least one order of magnitude less, but it forms such a small part of the overall cavity that its attenuation is not critical. Acoustic diffraction spreading in the cavity is a potential problem that has been partially alleviated by making the active electrode area as large as possible (the device should be mismatched for large Q) and by using crystal cuts in which the acoustic wave is at least partially self-collimating. Similarly, surface roughness and parallelism of the cavity must be addressed for optimal performance. With standard polishing techniques, their effect on the degradation in Q can be made negligible. The limiting factor in design and fabrication of high-Q HBARs is the ground plane metalization. Unfortunately, ZnO grows best on order (1, 1, 1) gold (the two lattices are evenly matched). Even though only .1 μm thick, the low Q of gold seriously degrades the overall device Q. Growing the piezoelectric layer directly on the substrate and using the LFE configuration is one possible solution to a higher Q.

11.7.2 Film Bulk Acoustic Resonators

HBARs have been fabricated to date as discrete devices with size determined by the acoustic cavity dimension. They are packaged individually and soldered into place. An increasingly important requirement in military electronic systems is for acoustic devices operating in the ultra high frequency (UHF) to microwave region that can be fabricated by

traditional very large scale integration (VLSI) technologies. The integration of piezoelectric devices into monolithic chip structures would permit dramatic reductions in size and weight. The FBAR structure consists of a transducer attached to a dead layer, as in the HBAR, but in which the nonpiezoelectric layer is either much thinner than, or of comparable thickness to, the piezoelectric layer (Figure 11.14). If the piezoelectric layer consists of sputtered ZnO, it can, at least theoretically, be formed as one step in a microwave integrated circuit manufacturing operation, which permits both large-scale fabrication and potentially very low cost. If the dead layers are significantly thinner than the piezoelectric transducer, the response of FBARs is similar to the simple quartz resonator, except that the dead layers usually play an important part and may significantly increase the C ratio of the composite structure if too thick. Such a structure is said to be nearly *edge-supported.* On the positive side, use of high coupling ZnO gives a dramatically lower C ratio as compared to quartz for the purely edge-supported structure (less than 20 as compared with 150 for quartz).

Typical applications of FBAR structures include oscillators and wideband filters. In the former application, the small size and high reliability of an integrated structure is more important than the moderate Q-factors (between 1000 to 3000 at 1 GHz) that can be attained. The Q limitation is due to the relatively high attenuation of ZnO and, more importantly, to the fact that the required gold metallic layer forms a large portion of the acoustic path. The latter application uses the relatively high coupling constant of ZnO.

From a fabrication perspective, the edge-supported structure has not been successful. Resonators operating at frequencies less than about 300 MHz require an inordinate amount of time to form the required half-wave thickness layer (ZnO sputters at only about 3 μm/h, so a 20-μm layer requires nearly 7 h). Further, such thick films tend to be highly stressed and invariably peel off the substrate. Thinner films can be formed unstressed but lack structural integrity, which compromises the overall reliability of the circuit.

To circumvent fabrication problems researchers have proposed a composite structure in which ZnO is grown on top of a hard support layer. The C ratio of the fundamental response is severely compromised if the support layer is more than 50% of the acoustic path. The degradation in the device FOM as a function of the thickness ratio between support and piezoelectric layers is shown in Figure 11.15 for ZnO on Si. The slight rise in FOM for small Si thicknesses occurs because Si has a lower acoustic attenuation than ZnO. As the Si thickness becomes appreciable, however, the C ratio rapidly deteriorates, thereby degrading the overall FOM.

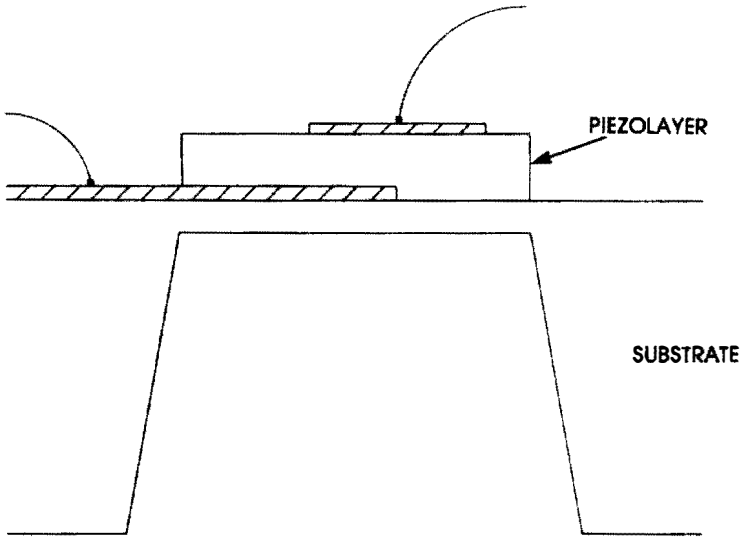

Figure 11.14 FBAR configuration. The piezoelectric and support layers are of comparable thicknesses. The response is quite strong in the second harmonic.

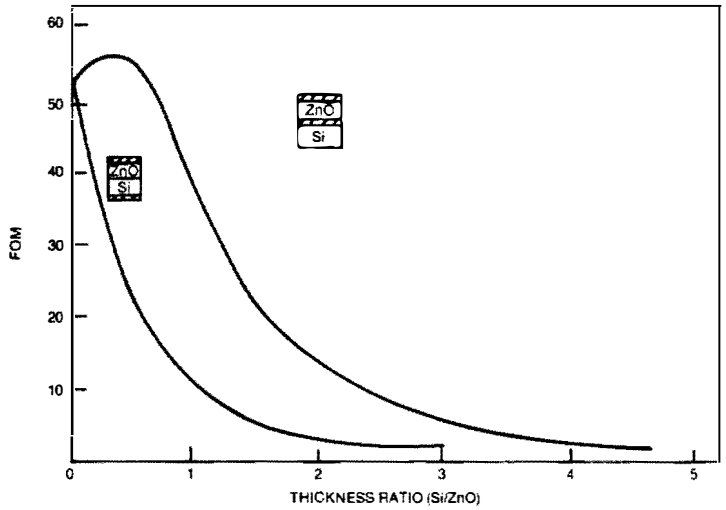

Figure 11.15 Figure of merit ($Q/2C_r$) of the fundamental response of an FBAR structure. As the thickness ratio increases, C_r increases dramatically and device performance rapidly degrades.

The composite resonator structure possesses a *second* harmonic response with C ratio, which can approach the edge-supported fundamental if the thickness of the support is properly chosen. Although even harmonics are completely suppressed in the edge-supported structure, they are present in composite resonators because the piezoelectric layer does not make up the entire resonating structure. For example, a small but noticeable second harmonic response can be seen in a metalized resonator even at low frequencies. Figure 11.16 shows the theoretical performance of a composite resonator consisting of ZnO on Si operating at 1 GHz in the fundamental and second harmonic modes. Although the second harmonic has no response in the edge-supported structure (zero thickness ratio), it does possess a wide peak near the normalized thickness ratio of unity (the thickness ratio is normalized with respect to the acoustic velocities). Note that the value of this peak is nearly equal to that of the fundamental in the edge-supported structure (without metalization layers!). The specific ratio and value of the peak strongly depend on the acoustic attenuations and material constants of the support layer. This dependence is illustrated in Figure 11.17, which shows the performance of a 1 GHz resonator for some important combinations of piezoelectric and support materials.

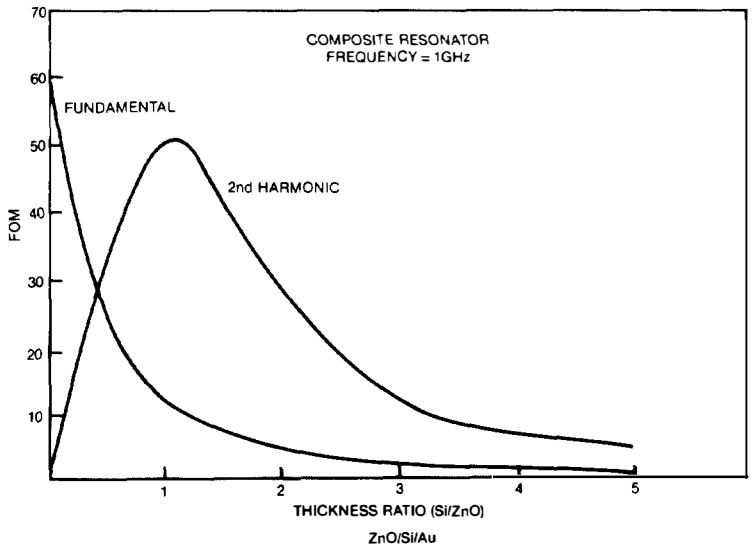

Figure 11.16 Figure of merit of FBAR second harmonic at 1 GHz. At a thickness ratio of about 1, the response is quite strong, making this structure useful for wideband filters.

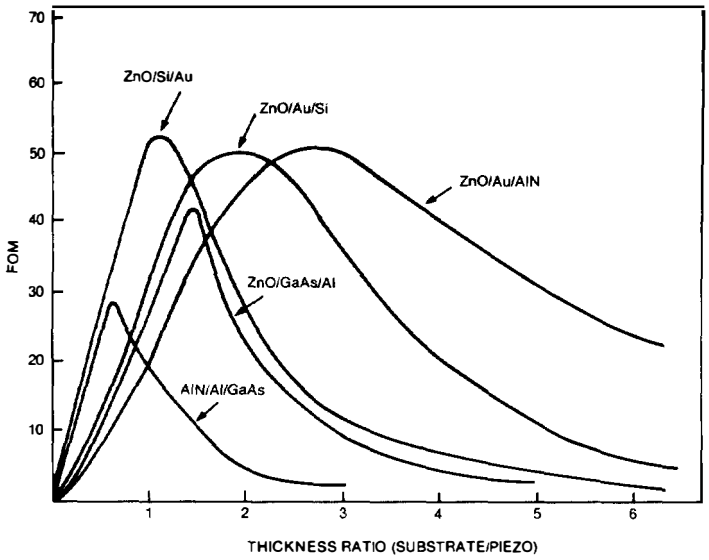

Figure 11.17 Performance of 1 GHz composite second harmonic FBAR structure for various piezoelectric layer–substrate combinations. Each case must be considered individually because of the wide variations in response.

Because the edge-supported configuration is identical to the classical resonator structure, a third harmonic exists for it. Like the resonator, however, the FOM for this case is much less than the fundamental due to the inverse-squared dependence of the coupling constant on harmonic mode number. Even at frequencies well in excess of 1 GHz, however, a composite structure can have very high performance. Computer modeling, for example, shows that a third harmonic composite structure of ZnO on Si or GaAs at 1.5 GHz has an FOM of 25, which is nearly equal to the fundamental edge-supported case. The piezoelectric layer thickness for the composite structure is 1.7 μm, and the Si support layer is 4 μm. For a 2-GHz device, a fourth harmonic configuration can be used. In this case, the ZnO layer is approximately 1-μm, and the Si layer is 5.3 μm. This design is relatively easy to fabricate with high reliability because of the thick support layer, and the performance is only 15% less than that in the edge-supported case.

Even if the composite structures did not give increased performance, there is an additional reason for their use. Theoretical calculations have shown that the fundamental mode, edge-supported ZnO on Si structure

is not energy-trapped. Measurements with fabricated devices confirm this computation and show that the Q and, especially, C ratio are much poorer than the one-dimensional model predicts. As we previously discussed, higher-order harmonics, however, are trapped. This is confirmed with measurements on fabricated devices, which show excellent correlation between theory and experiment for second and higher order harmonic structures.

11.7.3 Applications of Film Bulk Acoustic Resonators

Although film resonators have potential as frequency control elements in monolithic oscillators, their moderate-to-low Q-factors compared with single-crystal quartz may be a serious obstacle to large-scale utilization. On the positive side, the lower C ratio of film resonators allows more sophisticated frequency tuning and temperature compensation techniques, and their monolithic nature increases reliability. A more potentially important application in which the low C ratio is a critical advantage over quartz resonators is in the area of wideband multipole-crystal filters. In this application, the C ratio determines the achievable bandwidth, and a low Q will at most increase the insertion loss, IL. A typical three-pole ladder filter is shown in Figure 11.18. Each resonator represents one pole; the greater the number of poles the higher is the out-of-band rejection. The bandwidth, however, is determined solely by the C ratio of the individual resonators. In practice, the capacitors are fabricated in parallel with the acoustic resonators by using the same type of processes (e.g., RF sputtering). Active devices are fabricated on the same Si or GaAs chip, so the structure is entirely monolithic.

Each resonator in Figure 11.18(a) has a BVD equivalent circuit, as shown in Figure 11.18(b). As discussed previously, the values of the motional elements depend on the acoustic and electrical properties of the constituent FBAR layers. Once the equivalent circuit is known (by solving the Mason model), we can determine the overall filter response by standard *circuit* analysis techniques. Figure 11.19 shows, for example, the transfer response of a two-pole ladder filter using the Touchstone computer-aided analysis program. The individual FBAR resonators have the circuit values:

$$C_0 = 1.2 \text{ pF}, \quad C_m = .035 \text{ pF}, \quad L_m = 1400 \text{ nH}, \quad R_m = 3\Omega$$

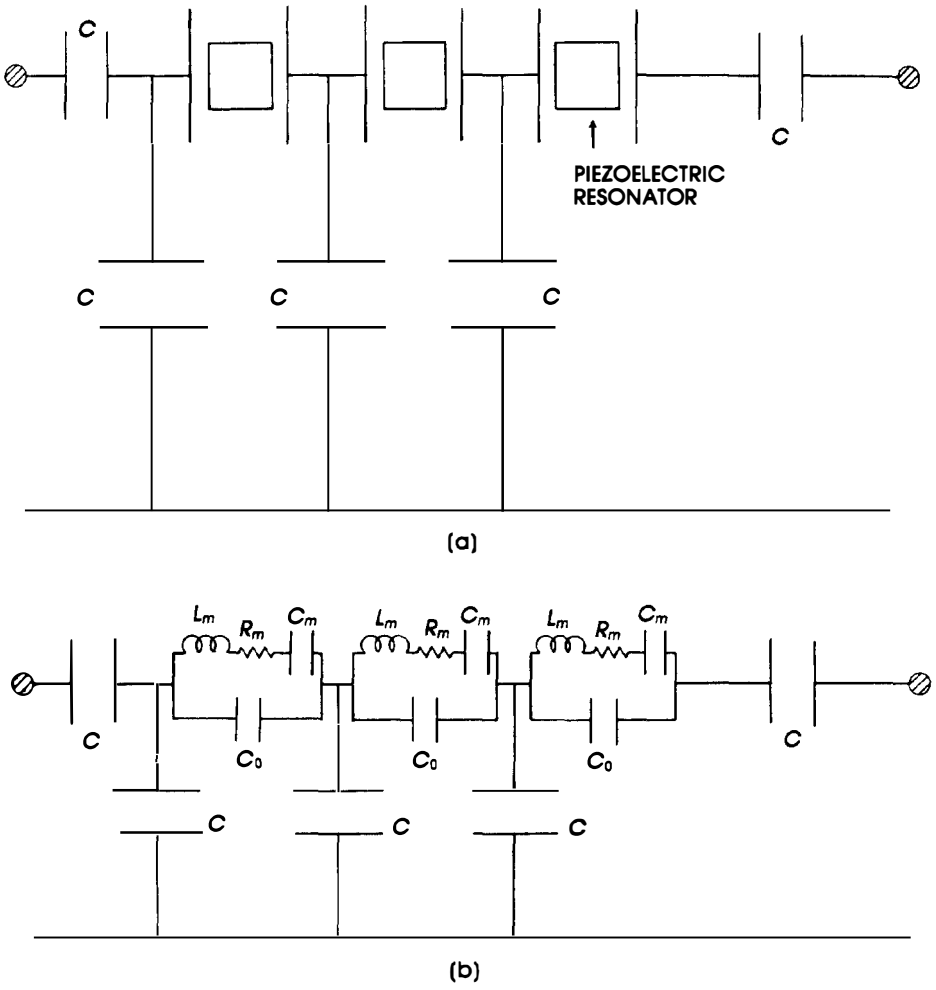

Figure 11.18 Three-pole crystal ladder filter: (a) schematic diagram showing overall structure; (b) diagram showing each resonator as a BVD equivalent circuit. *Note:* in this form, the filter response can be analyzed with standard circuit techniques.

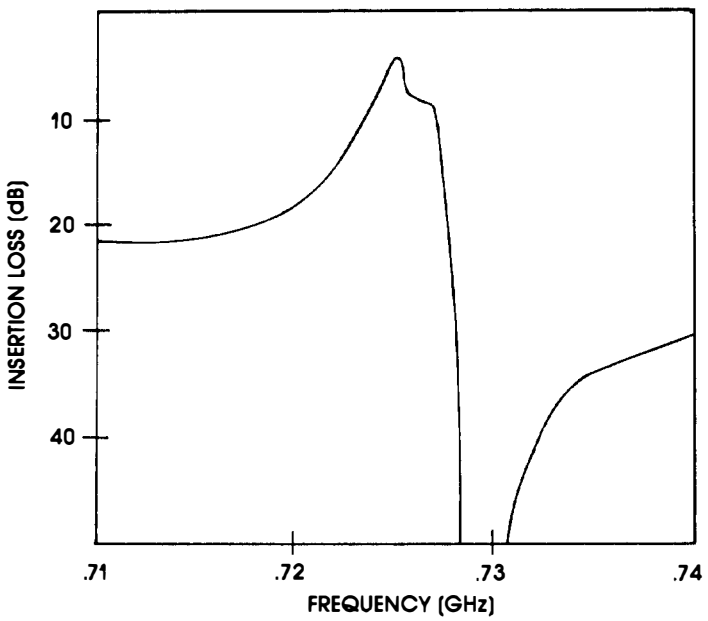

Figure 11.19 Transfer response of a two-pole ladder filter. Insertion loss (which depends on the resonator Q) is quite low, but the overall response is poor. Note the lack of symmetry and the antiresonance pole.

The series resonance frequency is 720 MHz, and the resonator Q is 2100. These values correspond to a second harmonic ZnO on Si FBAR, which is not particularly difficult to fabricate. The value of C_r for the acoustic resonators is

$$C_r = \frac{C_0}{C_m} = 34$$

The filter bandwidth is given by

$$\text{BW} = \frac{\omega_r}{2C_r} = 11 \text{ MHz}$$

Note that the bandwidth is independent of Q. From Figure 11.19, we see that the filter bandwidth is indeed close to 10 MHz. The device IL is quite low compared with a surface acoustic wave filter, but the out-of-band rejection does not compare favorably. Figure 11.20 shows the theoretical response of a four-pole filter using the identical resonators. Although IL and BW are similar to the two-pole case, the filter response has been dramatically improved. If the C ratio could be reduced to 17 (which is the theoretical value with the bulk coupling constant of ZnO), the bandwidth could be increased to over 20 MHz. The IL depends on the resonator Q, but if the resistance of the resonators is increased to, say, 30 Ω (reducing the resonator Q to only 200!), the IL increases only about 10 dB. Increasing the Q to 10^4 reduces the IL to less than 2 dB.

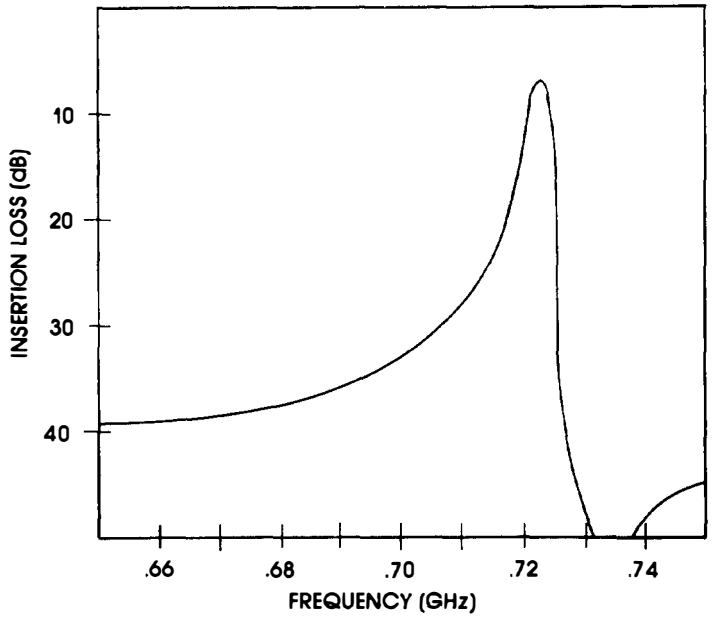

Figure 11.20 In a four-pole filter, the skirts are dramatically improved, but the antiresonance is still present.

We may further improve the filter response by "resonating" out the clamped capacitors through the use of "roofing" inductors, as shown in Figure 11.21. A clamped capacitance C_0 of 1.2 pF requires an L_0 of 40 nH at 720 MHz. It is possible to fabricate monolithically an inductor with this magnitude, but its resistance will be quite high, which may degrade the filter performance. The theoretical response is shown in Figure 11.22. Not only has the bandwidth increased, but also the response is nearly symmetric with no antiresonance.

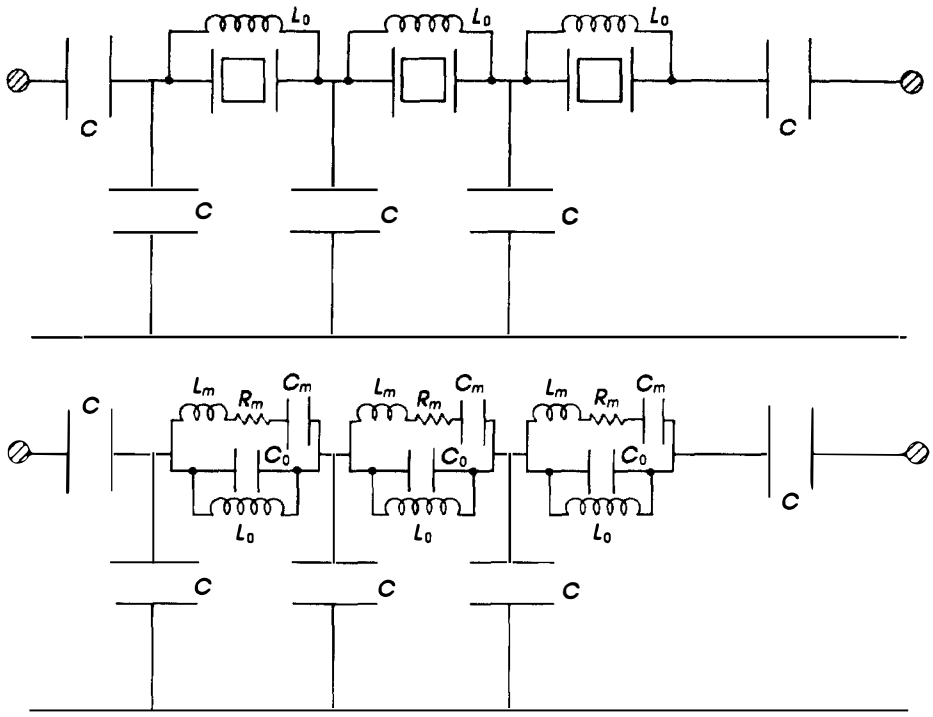

Figure 11.21 Schematic diagram of a three-pole filter with "roofing" inductors, which resonate the clamped capacitors: (a) schematic diagram; (b) BVD equivalent circuit.

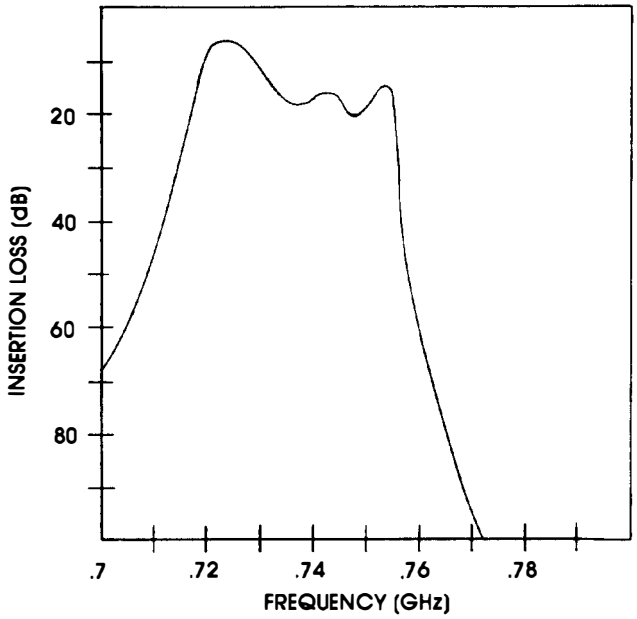

Figure 11.22 Four-pole filter response with roofing inductors shows a symmetric response.

PROBLEMS

11.1 We define resonance as the frequency for which the impedance characteristic crosses the real axis. Call this frequency ω_r' and show that its relation to ω_r (where $\omega_r = 1/(L_m C_m)^{1/2}$) is

$$\omega_r' = \omega_r\left(1 + \frac{C_r}{2Q^2}\right) = \omega_r\left(1 + \frac{1}{(\text{FOM})Q}\right)$$

For high-quality resonators, the difference is negligible.

11.2 If resonance is defined as the frequency for which the magnitude of the impedance is a minimum ω_r'', show that the relation between ω_r'' and ω_r is

$$\omega_r'' = \omega_r\left(1 - \frac{C_r}{2Q^2}\right) = \omega_r\left(1 + \frac{1}{(\text{FOM})Q}\right)$$

11.3 Find the possible coupling constants for the LFE of ⟨z⟩ $LiNbO_3$.

11.4 Repeat Problem 11.3 for ⟨z⟩ ZnO.

11.5 Derive (11.9), which expresses the plate normal of the ⟨*SC*⟩-cut in terms of the angles θ and ϕ.

11.6 Use the computer program for calculating the coupling constants (Chapter 4, Figure 4.4) to determine k_t^2 for the thickness-excited ⟨*SC*⟩-cut. The inputs to the program are (ϕ = 22.4)

abscissa: $\sin\phi\mathbf{i} + \cos\phi\mathbf{j}$ = (.381, .925, 0)
ordinate: (0, 0, 1)

The stress-compensated cut occurs when the angle as measured from the abscissa is 33.9°.

11.7 Consider an ⟨*AT*⟩ quartz resonator at 100 MHz with .5 μm Al metalization. Show that this structure has a small second harmonic response, then plot it on a Smith chart. Use the programs of Figures 6.12 and 11.1. Vary the thickness of the metalization and observe the response.

REFERENCES

1. M. Berté and P. Hartemann, "Quartz Resonators at Fundamental Frequencies Greater than 100 MHz," *Proc. 1978 IEEE Utrason. Symp.*, 148 (1978).
2. J. Aubry, "Quartz and $LiTaO_3$ Resonators for Direct Frequency Generation in the GHz Range," *Proc. 1983 IEEE Ultrason. Symp.*, 487 (1983).
3. A. Ballato and T. Lukaszek, "Mass Loading of Thickness-Excited Crystal Resonators Having Arbitrary Piezo-Coupling," *IEEE Trans. Sonics Ultrason.* **SU-21** (4), 269 (1974).
4. R. Besson, "A New 'Electrodeless' Resonator Design," *Proc. 31st Ann. Freq. Control Symp.*, 147 (1977).

5. R. Besson and U. Peier, "Further Advances on B.V.A. Quartz Resonators," *Proc. 34th Ann. Freq. Control Symp.,* 175 (1980).
6. E. Hatch and A. Ballato, "Lateral-Field Excitation of Quartz Plates," *Proc. 1983 IEEE Ultrason. Symp.,* 512 (1983).
7. A. Ballato, E. Hatch, M. Mizan, and T. Lukaszek, "Lateral Field Equivalent Networks and Piezocoupling Factors of Quartz Plates Driven in Simple Thickness Modes," *IEEE Trans. Ultrason. Ferro. and Freq. Control.* **UFFC-33** (4), 385 (1986).
8. A. Ballato, E. Hatch, T. Lukaszek, and M. Mizan, "Lateral-field Coupling of Rotated BAW Plates with $3m$, $4mm$ and $\bar{4}3m$ Symmetry," *Proc. IEEE 1986 Ultrason. Symp.,* 339 (1986).
9. W. Shockely, D. Curran, and D. Koneval, "Energy Trapping and Related Studies of Multiple Electrode Filter Crystals," *Proc. 17th Ann. Freq. Control Symp.,* 88 (1963).
10. E. Gerber, T. Lukaszek, and A. Ballato, "Advances in Microwave Acoustic Frequency Sources," *IEEE Trans. Microwave Theory Tech.* **MTT-34** (10), 1002 (1986).
11. R. Moore, J. Haynes, and B. McAvoy, "High Overtone Bulk Resonator Stabilized Microwave Sources," *Proc. 1981 Ultrason. Symp.,* 414 (1981).
12. T. Grudkowski, J. Black, T. Reeder, D. Cullen, and R. Wagner, "Fundamental Mode VHF/UHF Bulk Acoustic Wave Resonators and Filters on Silicon," *Proc. 1980 IEEE Ultrason. Symp.,* 829 (1980).
13. J. Rosenbaum, H. Salvo, and S. Krishnaswamy, "Overtone Response of Composite Bulk Acoustic Resonators," *Proc. 40th Ann. Freq. Control Symp.*, 206 (1986).
14. J. Rosenbaum, "Design of Ultra High Frequency Composite Piezoelectric Resonators," *Proc. Int. Conf. Ferroelectrics*, 296 (1986).
15. M. Driscoll, R. Moore, J. Rosenbaum, S. Krishnaswamy, and J. Szedon, "Recent Advances in Monolithic Film Resonator Technology," *Proc. IEEE 1986 Ultrason. Symp.,* 365 (1986).
16. T. Lukaszek, "Mode Control and Related Studies of VHF Quartz Filter Crystals, *IEEE Trans. Sonics and Ultrasonics,* **SU-18** (4), 238 (1971).